Research Square

Preprints are preliminary reports that have not undergone peer review.
They should not be considered conclusive, used to inform clinical practice,
or referenced by the media as validated information.

Perfusable Three-Dimensional Polyurethane (PU) Scaffold Platform Promotes Multicellular Tumor Spheroid (MCTS) Formation of U87 Glioblastoma for Tumor Microenvironment Modeling

Kevin L. Zhang
New York Institute of Technology
Rabab Hamzah
New York Institute of Technology
Jeffrey Chu
New York Institute of Technology
Matthew Duazo
New York Institute of Technology
Samuel Kaldas
New York Institute of Technology
Robert Griffin
University of Arkansas for Medical Sciences
Karrer Alghazali
kalghaza@nyit.edu

New York Institute of Technology

Article

Keywords: glioblastoma (GBM), tumor microenvironment (TME), three-dimensional scaffold (3D), polyurethane (PU), polymer beads, multicellular tumor spheroid (MCTS)

Posted Date: September 11th, 2026

DOI: https://doi.org/10.21203/rs.3.rs-10789864/v1

License: This work is licensed under a Creative Commons Attribution 4.0 International License.
Read Full License

Additional Declarations: No competing interests reported.

Abstract

Glioblastoma (GBM) is among the most lethal primary brain tumors, despite multimodal treatment. A significant barrier to the development of effective therapeutics is the inability of conventional two-dimensional (2D) culture systems to replicate the complex tumor microenvironment (TME). While three-dimensional (3D) models are able to capture the complexities of the TME, they are often constrained by suboptimal mechanical integrity, insufficient nutrient diffusion, and limited scalability.

To address this gap, we developed a porous polyurethane (PU) 3D scaffold designed to support long-term multicellular tumor spheroid (MCTS) formation. Our scaffold exhibited a homogeneous, interconnected pore architecture with an average pore size of approximately **250μm**, while possessing mechanical properties comparable to brain parenchyma (**G' = 862Pa; G" = 275Pa**). U87 GBM were seeded into pre-packed scaffold constructs and cultured for up to four weeks, after which spheroid formation and viability were assessed with a live/dead assay and two-photon microscopy. Additionally, the spheroids within the scaffold were also evaluated for drug effects with temozolomide (TMZ).

Within one week, the scaffold facilitated rapid cell attachment with early spheroid formation, and sustained long-term viability throughout four weeks, maintaining approximately 70–84% viability under optimized conditions. The porous architecture of the scaffold facilitated interconnected spheroid growth, while preserving structural integrity throughout the entirety of the culture. Additionally, treatment with 800μM TMZ caused a progressive reduction in spheroid viability to 67.9% and 61.3% at 24 and 48 hours respectively, demonstrating the platform's capacity to support a therapeutic effect.

Our scaffold platform offers a biomimetic, reproducible, and scalable 3D tumor model that supports long-term spheroid culture and quantitative drug evaluation. Its modular design is compatible with perfusion bioreactor systems, providing versatile applications for tumor microenvironment modeling and preclinical therapeutic screening.

1. Introduction

Glioblastoma (GBM), classified as a WHO Grade IV Astrocytoma, is the most prevalent primary malignant brain tumor in adults, accounting for approximately 52% of malignant primary brain tumors and 14% of all tumors in the United States [1]. Despite the advent of concurrent chemoradiotherapy with temozolomide (TMZ) the current standard of care the median overall survival remains roughly fifteen months from diagnosis, with five-year survival rates at roughly 7% [2, 3]. The poor clinical prognosis of GBM is attributable to intratumoral heterogeneity, hypermutation, and immunosuppression within the tumor microenvironment (TME), contributing to aggressive, diffuse infiltrative growth that is markedly resistant to conventional therapies [4].

The majority of preclinical research on GBM, as well as other malignancies, has relied on conventional two-dimensional (2D) cell culture systems, in which tumor cells are expanded as monolayers on plastic platforms. While indispensable for mechanistic investigations of cellular proliferation, gene expression,

and drug cytotoxicity, these systems are fundamentally limited in their capacity to represent the complexity of GBM in vivo [5]. The TME of GBM involves malignant cells in continuous communication with stromal cells (fibroblasts, endothelial cells, extracellular matrix, etc.), vasculature, lymphatic tissue, and immune effector cells (T-cells, B-cells, macrophages, etc.), which drives aggressive tumor growth, invasion, and metastasis through angiogenesis, metabolic adaptation, and immune evasion [6]. In a monolayer culture, cells are deprived of spatial geometry, contact adhesion, and extracellular matrix interactions. Thus, the absence of these metabolic, nutrient, and signaling gradients renders 2D models poor predictors of clinical drug response, contributing to the translational discrepancy between preclinical drug efficacy and clinical trial outcomes, which underlies the high attrition rate in pharmacological therapeutic development [7, 8]. These limitations have prompted the development of physiologically relevant models that attempt to accurately model the three-dimensional architecture and dynamics of the TME.

Consequently, the increasing utilization of three-dimensional (3D) cell-culture systems has allowed for improved approximation of spatial organization, cell-cell contact interactions, and diffusion dynamics of native tumor tissue cytoarchitecture [9, 10]. The current landscape of 3D platforms features hydrogels, spheroids, organoids, scaffolds, and microfluidics, with each approach modeling distinct aspects of tumor biology while possessing its own strengths and limitations, particularly in terms of reproducibility, and scalability, and throughput. Of these systems, hydrogels are often utilized to grow tumors, while mimicking biological environments [11]. They are fabricated through the crosslinking of natural, synthetic, or hybrid polymers, resulting in hydrophilic networks that swell in aqueous media to form porous, “fluid-like” gels that resemble the cell-matrix interactions of natural tissue [12, 13]. The primary strength of hydrogel matrices is the capacity for modification, enabling independent control over biodegradability, porosity, and stiffness [14–16]. However, the primary limitation is a lack of structural stability, as hydrogels are susceptible to proteolytic degradation by matrix metalloproteinases (MMPs), leading to gel remodeling, contraction, and collapse [17]. These outcomes often introduce confounding effects that fail to accurately reflect the long-term dynamics of TMEs.

Multicellular tumor spheroids (MCTSs) have also emerged as an accessible platform for capturing the architecture of solid tumors. MCTSs are self-assembled aggregates of tumor cells, typically formed in non-adherent conditions, including ultra-low attachment growth plates, hanging drop arrays, spinner flasks, or rotary bioreactors [18–20]. This self-aggregation of cells promotes the development of transport gradients, driving the formation of concentric zones, specifically a proliferating outer rim, a quiescent intermediate zone, and a central hypoxic core [21, 22]. The primary strength of MCTSs is the ease of reproducibility, with well-established protocols for a multitude of cell lines, including GBM [23, 24]. However, the primary limitation is the lack of structural stability, particularly as they reach the diffusion growth limits which often leads to collapse [25].

Tumor organoids have been utilized to preserve the diverse genetic features of real tumors. Organoids are self-assembled aggregates of tumor cells, typically derived from patient tissue [26]. The primary strength of organoids is the capacity to capture the genetic heterogeneity of a patient’s tumor, allowing

for individualized treatment. Additionally, organoids are a superior alternative to patient-derived xenografts (PDXs) by utilizing human cells, thereby minimizing the confounding effects associated with interspecies differences [27]. Furthermore, the advancement of organoids has allowed for the establishment of biobanks for a multitude of tumor cell lines, including GBM [28–32]. However, the primary limitation is the resource- and time-intensive requirements, involving access to tumor biopsies, complex culture protocols, and low culture efficiency and yield, all of which limit experimental throughput [33]. Additionally, organoids are subject to the exact structural and growth constraints as spheroids. For spheroids and organoids, the absence of a scaffold matrix limits their ability to recapitulate the structural and biochemical interactions characteristic of the TME.

Biomimetic scaffolds have emerged as a scalable platform for engineering the spatial architecture of the TME. The fabrication of scaffolds encompasses an extensive spectrum of materials and designs, including electrospun fibers, decellularized tissue, annealed beads, bioprinted matrices, among others [34, 35]. Among these systems, scaffolds are distinguished by their capacity for modification of porosity, mechanical integrity, and degradation kinetics [36, 37]. However, the primary limitation is the non-transparency of the large majority of biomaterials, which introduces optical opacity and light scattering, preventing effective analysis of cellular dynamics [38].

Lastly, organ-on-chips (OOCs) have been utilized for assessing the spatiotemporal dynamics of the TME. OOCs are predominantly fabricated through “soft lithography,” which involves etching microfluidic channels into biomaterials to produce a miniature functional tissue environment [40]. The etching of a silicon substrate with liquid polymers produces microchannels, at a micrometer to nanometer scale, within a matrix, enabling the controlled delivery of oxygen, nutrients, and therapeutics. The primary strength of OOCs is the ability to impose predefined biophysical parameters at a spatiotemporal resolution unmatched by any other system [41]. Additionally, the real-time integration of electrochemical and optical sensors allows for continuous, non-destructive assessment of constructs [42]. However, the primary limitation is the resource- and time-intensive requirements, involving access to lithography and microfluidics equipment as well as micro-surface treatment protocols, all of which limit experimental throughput [43].

Across existing systems, three interconnected challenges have emerged as limitations for advancing tumor models. First, the lack of adequate diffusion imposes a ceiling on the size; without active oxygen and nutrient delivery, constructs begin exhibiting necrosis, thereby failing to sustain viable tumors [25, 44]. Second, the lack of structual stability imposes a ceiling on tumor migration, infiltration, and remodeling dynamics [45]. And third, the lack of reproducibility and scalability imposes a ceiling on high-throughput experimentation, often required for therapeutic screening applications [33, 46]. Thus, addressing these challenges requires an engineered platform that integrates: 1) Porosity and Perfusability, 2) Mechanical Integrity and Structural Stability, and 3) Reproducibility and Scalability.

In the current study, we address these challenges by introducing a novel scaffold platform that provides tumor spheroids with a stable environment, capable of sustaining long-term growth, in which porosity,

perfusability, and structural stability can be independently optimized. We demonstrate that our scaffold offers long-term structural stability, with a controlled porosity that enables cell attachment, infiltration, and proliferation, while facilitating oxygen and nutrient transport through static-phase characterizations, followed by optimized seeding of U87 GBM. Our findings establish a proof-of-concept for our scaffold platform, establishing the experimental foundation for future co-culture investigations as well as perfusion bioreactor integration.

2. Materials and Methods

2.1 Polymer Bead Fabrication

Our scaffold was fabricated from a biodegradable polyurethane (PU) composite. A 10% (Weight/Volume) D4 PU (Advance Source Biomaterial) Solution was prepared in a 90:10 (Volume/Volume) ethanol/deionized water (EtOH/DIW) mixture to serve as a polymer precursor. In order to introduce porosity, sodium chloride (NaCl) was incorporated into the polymer solution with a mechanical mixer (SMX-5000-9 Bone Cement Mixer Bowel) at a ratio of 50g NaCl per 1g of PU, yielding a viscous composite mixture. The NaCl was gradually added under continuous mixing in order to ensure homogeneous dispersion throughout the polymer matrix.

Immediately following mixing, the viscous polymer-salt composite was packed into glass molds, and then immersed into a bath of pyrogen-free DIW, which induced a salt-assisted phase inversion, driven by solvent-nonsolvent exchange as well as initiated porogen leaching, causing formation of a porous scaffold. The scaffold was immersed in the water bath for seven days, with periodic changes of DIW every six to twelve hours in order to ensure complete removal of residual solvent and salt. Upon completion, the scaffold exhibited a highly interconnected, porous architecture, and was collected for processing.

The bulk porous scaffold was manually sectioned into smaller fragments with sterilized scissors, before being transferred into a blender filled with DIW, and subjected to short-pulse blending cycles to generate porous beads. Blending parameters, including pulse duration and processing time, were optimized for size distribution, while preserving pore architecture. The beads were stored in and washed with sterile phosphate-buffered saline (PBS) under laminar flow, followed by overnight irradiation within a biosafety cabinet. Prior to scaffold assembly, an analysis of porosity, surface morphology, and mechanical integrity was performed through micro-computed tomography (MicroCT), three-dimensional optical profilometry, and viscoelasticity testing, respectively, as depicted in Fig. 1.

2.2 Scaffold Characterization and Testing Methodology

Prior to scaffold assembly, porous polyurethane (PU) beads were comprehensively characterized to evaluate their structural, morphological, and mechanical properties. Three complementary analytical

techniques were employed: micro-computed tomography (MicroCT), three-dimensional (3D) optical profilometry, and non-contact viscoelasticity testing.

2.2.1 Micro-Computed Tomography (MicroCT)

PU scaffolds were evaluated using high-resolution micro-computed tomography (MicroCT) imaging (SkyScan 1173, Bruker; voxel size 0.017 x 0.017 x 0.017; matrix size 2240 x 2240) with a voltage of 80 kV, current of 100 uA, and exposure of 740 ms. Scans were reconstructed using NRecon (version 1.7.4.6; Micro Photonics Inc.). Samples were scanned to obtain three-dimensional reconstructions of the scaffold structure without destructive sectioning. MicroCT images were analyzed via Dragonfly 3D World (version 2025.1; Comet Technologies Canada Inc.). Quantitative analysis was performed to determine total porosity (%), pore size distribution, pore interconnectivity, and scaffold thickness. Three-dimensional renderings were generated to visualize the internal pore network and assess the uniformity of the fabrication process.

2.2.2 Three-Dimensional Laser Confocal Microscopy

Three-dimensional surface morphology of the scaffolds was characterized using a Keyence VK-X laser confocal microscope (Keyence Corporation, Osaka, Japan). The non-contact 661 nm laser confocal system was used to obtain high-resolution 3D images of the porous scaffold architecture without damaging the samples. Scaffolds were imaged in the hydrated state to mimic cell culture conditions. Surface morphology, including pore structure, surface roughness, and height profiles, was analyzed using the instrument's integrated analysis software under identical imaging conditions for all samples.

2.2.3 Viscoelasticity Testing

Stiffness and viscoelastic properties of the scaffold were measured using ElastoSens™ Bio. The device provides measurements of the Storage modulus (G'), loss modulus (G''), and damping factor (tan δ). Samples were tested in the hydrated state at 37°C to replicate physiological conditions. Multiple hydrated samples were analyzed to determine fabrication consistency.

2.2.4 Contact Angle Measurement

The wettability of the porous scaffolds was evaluated using a MSE PRO Laboratory contact angle goniometer. Static water contact angles were measured at room temperature by placing a droplet of deionized water onto the scaffold surface, and the contact angle was determined using the instrument's image analysis software. Measurements were performed at multiple locations on each sample, and the average value was reported to assess surface hydrophilicity.

2.2.45 SEM Sample Preparation and Imaging

Wet polyurethane (PU) bead scaffolds were frozen at − 80°C prior to lyophilization using a Labconco freeze dryer. Freeze-drying was employed to remove water while preserving the three-dimensional porous microstructure and minimizing collapse of the pore network. The dried scaffolds were mounted

onto aluminum specimen stubs using conductive carbon adhesive tape and sputter-coated with a thin layer of gold to enhance surface conductivity and reduce charging artifacts during imaging. Hitachi 4800 Scanning electron microscopy (SEM) at Brookhaven National Laboratory, Center for Functional Nanomaterials was used to collect the data. SEM was performed at an accelerating voltage of 5 kV using secondary electron imaging to characterize the scaffold morphology, pore size, pore interconnectivity, and surface microstructure.

2.3 Scaffold Assembly

The beads were packed into individual wells of six-well tissue culture plates (Cat. 3516, Corning, Corning, USA), which were lined with a microscope cover slip prior for subsequent imaging with water immersion two-photon microscopy. Approximately 100-150mg of beads were deposited per well and gently tamped with a sterile flat-tipped spatula to achieve uniform packing density, forming three-dimensional scaffolds approximately 3mm in thickness and 35mm in diameter, corresponding to the inner diameter of the six-well plate.

2.4 Cell Culture

Human GBM U87 MG (ATCC HTB-14) were thawed from liquid nitrogen storage and maintained in DMEM (Cat. D6421, Millipore Sigma, Burlington, MA, USA), supplemented with 10% Fetal Bovine Serum (Cat. MT25000CI, Corning) and 1% Penicillin–Streptomycin (Cat. 15140122, Gibco, Grand Island, NY, USA), and cultured at 37ºC at 5% CO_2. These cells were allowed at least two passages after thawing, and not maintained for more than ten passages before an experiment. 1×10^6, 5×10^6, and 10×10^6 Cells per Scaffold were seeded into the scaffold constructs, and cultured for up to four weeks, with daily media replacement. An analysis of cell attachment, spheroid formation, and long-term viability were assessed using a live/dead assay and two-photon microscopy at pre-specified timepoints.

2.5 Culture Timeline and Experimental Timepoints

In order to comprehensively assess the temporal dynamics of cell attachment, spheroid formation, and long-term viability of U87 GBM, scaffolds were evaluated at four experimental timepoints: 48 Hours, 1 Week, 2 Weeks, and 4 Weeks, as summarized below in Table 1. Triplicate scaffolds (n = 3 per Timepoint) were designated at the outset and plated on individual six-well plates for analysis at each scheduled timepoint without disturbance of scaffolds allocated to the other timepoints.

Table 1. Experimental timepoints and their corresponding biological objectives and primary outcome measures

Timepoint	Biological Objective	Primary Outcome Measure
48 Hours	Initial Cell Attachment and Early Scaffold Colonization	Cell Attachment Efficiency
1 Week	Early Multicellular Aggregate and Spheroid Formation	Aggregate Size; Viability; Bead Bridging
2 Weeks	Spheroid Maturation and Spatial Organization	Spheroid Diameter; Spatial Distribution
4 Weeks	Long-Term Spheroid Viability and Structural Stability Within Scaffold	Sustained Spheroid Viability; Spheroid Integrity

2.6 Live/Dead Viability Assay

At each timepoint, the scaffolds were removed from incubation and media was aspirated with a pipette. Afterwards, the scaffolds were rinsed twice with sterile PBS in order to remove residual media as well as non-adherent cells. Then, the scaffolds were treated with a LIVE/DEAD Viability/Cytotoxicity Kit (Cat. L3224, Invitrogen, Carlsbad, CA, USA) solution according to the manufacturer's guidelines: 5µL Calcein-AM and 20µL Ethidium Homodimer-1 per 10mL PBS. Approximately 2mL per Scaffold of solution was applied directly to the scaffolds and incubated at 25ºC for 1 hour, protected from direct light. Following incubation, the solution was aspirated with a pipette. A flat-tipped spatula was inserted underneath the cover slip and the scaffold was lifted and transferred to a petri dish.

Fluorescence imaging was performed using a two-photon confocal microscope (Zeiss Axio Examiner.Z1 2-P LSM, Carl Zeiss Microscopy GmbH, Jena, Germany). A series of z-stack images were acquired through a depth of 100–500µm from the scaffold surface using a 20x water immersion objective for high-resolution spheroid imaging, as summarized in Fig. 2. Image analysis was performed using Fiji/ImageJ. For each timepoint, spheroid size was measured as the maximum cross-sectional diameter identified within a z-stack. Subsequently, cell viability was quantified as the percentage of live cells relative to the total cell count (live + dead) across a minimum of six representative fields per timepoint.

2.7 Statistics and Data

All experimental data are presented as mean ± standard deviation (SD), unless otherwise stated. No statistical methods were used to predetermine sample size. Statistical analysis was performed on GraphPad Prism 11. Schematic figures were generated with GraphPad Prism 11, BioRender201 (biorender.com), and FigureLabs (figurelabs.ai).

3. Results

3.1 Scaffold Architecture Provides Micro-Environment That Supports Spheroid Formation

MicroCT analysis confirmed a highly porous structure with well-defined micropores distributed uniformly throughout the scaffold, with a dominant pore size of approximately 0.23 mm (Fig. 3A). This consistent micropore architecture indicates the interconnected porosity of the scaffold, ensuring optimal nutrient and oxygen diffusion. 3D laser microscopy revealed a continuous network of micro-peaks and valleys extending from the outer surface to the core (Fig. 3B). This topography creates an extensive network of interstitial spaces, dramatically increasing the available surface area for cell adhesion and supporting rapid, stable spheroid formation. The mean pore spacing was about 250 μm, with an average surface roughness of 1.87 μm, both of which are ideal for promoting cell attachment and growth.

To determine clinically relevant mechanical properties for the porous beads, we tested fresh cow brain tissue (from a local butcher) using the ElastoSens™ Bio system. The results of the brain tissue indicate G’ = 647 Pa and G” = 288 Pa (Fig. 3D). The initial scaffold prototypes were tested, and we selected the samples that most closely matched the target value. The selected prototype had a shear storage modulus (G’) of 862 Pa and a shear loss modulus (G”) of 275 Pa (Fig. 3C), which also closely mirrored the mechanical environment of brain parenchyma as reported previously [47]. Scanning electron microscopy revealed that the polyurethane (PU) bead scaffold possesses a highly porous and interconnected three-dimensional architecture (Fig. 3F). At low magnification (30×), the scaffold exhibited a homogeneous distribution of pores throughout the structure with no evidence of large voids or pore collapse, indicating successful fabrication and preservation of the porous network. The interconnected pore structure extends across the entire scaffold, suggesting continuous pathways that are favorable for nutrient transport, oxygen diffusion, and cellular infiltration. Higher-magnification SEM images (100×) further demonstrated the morphology of the pore walls, which consist of thin polymeric membranes interconnected by continuous struts. The pores exhibit an irregular but open morphology with interconnected windows of varying sizes, producing a highly permeable network. The pore surfaces appear relatively rough with microscale surface features, which may enhance protein adsorption and promote cell attachment. Collectively, these results provide strong evidence that the scaffold offers superior porosity, excellent perfusability, and outstanding mechanical stability, making it well-suited to withstand dynamic culture conditions and to foster an optimal environment for spheroid formation.

3.2 Scaffold Supports Long-Term Viability of Spheroids Throughout Four Weeks

3.2.1 Cell Attachment Observed at 48 Hours

Two-Photon Microscopy established that our scaffold platform supports consistent spheroid formation with substantial cell viability across all experimental timepoints. As observed in Fig. 4, overall cell viability was high, with Ethidium Homodimer-1 red fluorescing dead cells comprising only a small

percentage of the spheroids, while Calcein-AM green fluorescing viable cells comprised the majority of the spheroids. At forty-eight hours, live/dead imaging revealed extensive colonization of the scaffold, with cells attached to beads as isolated individuals and compact clusters, as depicted in Fig. 5B. These clusters ranged from 30μm to 120μm. The mean cell viability within the scaffold was 73.39 ± 4.16% for a concentration of $1x10^6$, 61.65 ± 4.43% for a concentration of $5x10^6$, and 75.07 ± 6.88% for a concentration of $10x10^6$ at 48 Hours, as depicted in Fig. 5A. These viability values indicated that there was minimal cytotoxicity associated with the scaffold biomaterials composition or cell seeding procedure. Additionally, cell infiltration depth, which was measured from confocal z-stacks, extended throughout the scaffold, demonstrating an extensive three-dimensional distribution of cells. In contrast, all controls exhibited extensive loss of cell viability by 1 Week, attributable to apoptosis triggered by loss of cell adhesion.

3.2.2 Early Spheroid Formation Observed at One Week

At one week, a striking reorganization of the cells was evident within the scaffold. The individual clusters of cells observed at forty-eight hours had progressed to coherent multicellular aggregates, consistent with the early stages of spheroid formation [48]. As expected, aggregates were observed bridging adjacent beads, forming multi-bead clusters in which cells occupied the interstitial space between beads — a configuration which leveraged bead curvature for aggregate growth (Fig. 5B). These aggregates ranged from 80μm to 200μm. The mean cell viability within the scaffold was 79.25 ± 4.66% for $1x10^6$, 61.60 ± 9.81% for $5x10^6$, and 83.90 ± 2.49% for $10x10^6$ at 1 Week (Fig. 5A). While there were slight increases and decreases in cell viability, these variations are statistically non-significant from forty-eight hours, attributable to the expected initial adaptation of cells to the scaffold. The formation of bead-bridging aggregates was a consistent and reproducible feature of the one week timepoint, observed across all three concentrations. The cells within the scaffolds exhibited a predominantly circular/spherical morphology with minimal cytoplasmic extensions, consistent with the aggregation driven compaction of early spheroid formation [49]. Furthermore, z-stacks confirmed that the aggregates extended through the full depth of the scaffold.

3.2.3 Spheroid Growth and Maturation Observed at Two Weeks

At two weeks, the aggregates observed at one week had become larger, cohesive spheroids. These spheroids ranged from 150μm to 350μm. The mean cell viability within the scaffold was 73.69 ± 5.32% for $1x10^6$, 77.15 ± 4.21% for $5x10^6$, and 72.69 ± 3.99% for $10x10^6$ at 2 Weeks, as depicted in (Fig. 5A). Of note, z-stacks revealed live cells predominating in the outer shells, with an increase in dead cells detectable within the cores, consistent with the diffusion-limited necrosis that occurs within spheroids as well as tumors [25, 50]. Additionally, there were several spheroids within the scaffolds observed expanding beyond single bead-bead spaces to fill larger multi-bead interfaces, exhibiting irregular, lobulated morphology, reflecting spheroid growth constrained and molded by the scaffold architecture (Fig. 5B). This scaffold-directed spheroid morphology is a distinctive feature of our bead-based scaffold

platform; in contrast to suspension spheroids that form uniformly spherical aggregates, spheroids within our scaffold adopt architectures that incorporate the physical topology of the adjacent pore network, potentially recapitulating the irregular tumor growth patterns observed in vivo to a greater extent.

3.2.4 Long-Term Spheroid Viability Observed at Four Weeks

At four weeks, the spheroids persisted within the scaffold with enduring viability and structural integrity. These spheroids ranged from 250μm to 400μm. The mean cell viability within the scaffold was 84.11 ± 4.69% for $1x10^6$ and 71.98 ± 7.52% for $5x10^6$ (Fig. 5A). Of note, imaging and data collection was not performed on $10x10^6$ Cells/Scaffold at 4 Weeks, as the spheroids began to deteriorate and exhibit irregular morphologies, likely attributable to severe nutrient starvation, localized hypoxia, and cytotoxic waste accumulation within the packed scaffold constructs over the extended culture period [24]. Additionally, the considerable increase in cell death at 2 Weeks indicated that $10x10^6$ Cells/Scaffold was less optimal for spheroid development compared to $5x10^6$ Cells/Scaffold, which informed our decision for termination. Nevertheless, z-stacks revealed concentric zonation of the spheroids as observed in Week 2. Across all four timepoints, spheroid growth and cell viability followed a reproducible trajectory across independent scaffold triplicates. These results are consistent with previously published values for independent spheroid models of U87 GBM, which typically range from 70–90% in cell viability [51, 52].

3.3 Temozolomide Treatment Elicits a Cytotoxic Response in U87 GBM Spheroids

As previously discussed, temozolomide (TMZ) — a cytotoxic alkylating agent — has been the standard-of-care chemotherapeutic for GBM [2]. U87 GBM is a well-characterized in vitro cell line known for its intrinsic resistance to alkylating chemotherapeutic agents, including TMZ, primarily due to enhanced detoxification and genomic repair mechanisms [53]. Therefore, our scaffold was employed to systematically assess spheroid sensitivity to TMZ.

Based on spheroid distribution and density, the $5x10^6$ Cells per Scaffold at 2 Weeks was selected. Three triplicates were plated on individual six-well plates and following the two week culture period, an 800μM TMZ solution was added to two triplicates with an 800μM DMSO solution being added to the last triplicate to serve as a control. Afterwards, cell viability was assessed using the live/dead assay and two-photon microscopy at 24 Hours and 48 Hours following drug administration in order to enable comparative evaluation of drug efficacy over time. At twenty-four hours, cell viability decreased to 67.96 ± 3.60%, which progressively decreased to 61.26 ± 2.33% at forty-eight hours, as depicted in Fig. 6.

4. Discussion

In this study, we investigated the formation, development, and long-term viability of U87 GBM spheroids within a porous bead-based PU scaffold, and found that our scaffold platform promotes spheroid formation, while preserving viability over a four-week culture period, thus establishing the feasibility of our platform for preclinical and translational cancer research. The formation of intact spheroids within our scaffold recapitulates key aspects of in vivo glioblastoma growth within the brain parenchyma, particularly progressive three-dimensional organization and expansion.

Our scaffold characterization revealed structural and mechanical properties that align well with established parameters for effective 3D glioblastoma culture systems. The observed pore network, with an average diameter of 230 μm, falls within the optimal 200–400 μm range previously identified for supporting both nutrient transport and three-dimensional tissue architecture. This finding is consistent with recent work by Delattre et al., who demonstrated superior GBM cell accumulation and retention using 225 μm pores in macroporous hydrogels [54].

The mechanical properties of our scaffold represent a particularly significant achievement in biomimetic design, in our opinion. The measured storage modulus (G’ = 862Pa) and loss modulus (G” = 275Pa) closely approximate those of native brain tissue (G’ = 647Pa and G” = 288Pa), addressing a critical limitation in current GBM modeling approaches. This mechanical similarity is not merely desirable but essential, as glioblastoma cells exhibit pronounced mechanosensitive behaviors [55]. Previous studies have demonstrated that matrix stiffness directly influences GBM cell proliferation, migration patterns, and therapeutic resistance through mechanotactic pathways [56].

The surface topography, characterized by 1.87 μm roughness and regular pore spacing, likely contributed to the rapid spheroid formation observed within the first week of culture. This three-dimensional architecture provides a more physiologically relevant platform than conventional plastic culture systems, potentially improving the translational relevance of preclinical drug screening studies [57]. In future iterations, we are planning to add stromal cells to increase the relevant cell-cell communication involved in tumorigenesis and response to therapeutic treatments.

Although the viability for $5x10^6$ Cells per Scaffold was initially lower at the 48 Hour and 1 Week timepoints, viability increased by 2 Weeks. Furthermore, the distribution and density of spheroids throughout the scaffold were substantially greater than other conditions; however, the full extent of this observation could not be captured with two-photon imaging due to its limited field of view. This led to the determination that $5x10^6$ Cells per Scaffold for 2 Weeks was the optimal culturing condition for MCTS formation within our scaffold, consistent with previous findings that establish a limit of approximately fourteen days for spheroid culture under static conditions due to diffusion and nutrient limitations [44, 49]. Although TMZ treatment reduced spheroid cell viability, the observed drug response was less pronounced than anticipated. This decline in effect may be attributed to multiple factors, including potential drug absorption by the scaffold matrix and/or restricted diffusion, though studies show conflicting evidence regarding the role of diffusion limitations versus cell-matrix interactions in determining drug responsiveness [58, 59].

These findings reveal the inherent limitations of passive culture systems in supporting long-term spheroid growth, which have been widely documented across tumor spheroid models, and which is not unique to our platform. In order to accurately model the vascularized tumor microenvironment, active perfusion is required to facilitate continuous oxygen and nutrient delivery as well as metabolic waste clearance throughout the construct. Cell culture systems with active perfusion have been shown to enhance cellular viability, tissue volumes, and oxygen gradients [60, 61]. The modular architecture of our beads scaffold makes it inherently compatible with integration into perfusion bioreactors, microfluidic platforms, and organ-on-chip (OOC) systems, providing a clear pathway for future development. One of the key transformative applications of our platform lies in its integration with perfusion bioreactor systems to create a fully perfusable tumor microenvironment models — a direction that we are actively exploring.

Beyond improving long-term viability, perfusion bioreactors may also enhance the predictive value of our platform for therapeutic drug screening. The attenuated response to TMZ observed in the present investigation highlights the complex interplay between drug transport, scaffold interactions, and therapeutic response. The reduction in therapeutic efficacy has been reported in MCTSs, where limited drug penetration and microenvironmental heterogeneity contribute to treatment resistance when compared to conventional monolayers [62]. The incorporation of controlled perfusion could improve the reproducibility of drug exposure throughout the construct.

There are several limitations of the present investigation which should be acknowledged. Our platform was evaluated using a single cell line (i.e. GBM U87), and future investigations should examine alternative immortalized cell lines as well as patient-derived cell lines. Additionally, imaging of the scaffold was constrained by the field of view and penetration depth of two-photon microscopy, limiting comprehensive quantification of spheroid distribution throughout the entire construct. Furthermore, although cell viability was assessed, molecular characterization of hypoxia, proliferation, and resistance markers was beyond the scope of our investigation, and represents an important direction for future investigations. The role of stromal cells, including endothelial, fibroblast, or immune cells in these aspects of a developing tumor microenvironment can also be assessed with the newly developed scaffold approach. Any future investigations should also focus on exploring microenvironmental remodeling dynamics, incorporating other cell populations as well asculturing patient-derived organoids.

5. Conclusion

This study shows that a porous bead-based polyurethane scaffold can reliably support long-term growth of U87 GBM spheroids. The scaffold worked best with 5×10^6 cells per scaffold over two weeks, and the cells stayed alive for up to four weeks. Its structure and mechanics are very similar to real brain tissue: the average pore size is 230 μm, which is good for getting nutrients in and letting cells grow in 3D, and its stiffness (862 Pa storage modulus, 275 Pa loss modulus) is close to actual brain tissue (647 Pa and 288 Pa).

These features help solve key problems with current GBM models, since the stiffness of the scaffold affects how glioblastoma cells behave [51, 63]. Spheroids formed quickly in the first week and kept growing and organizing in 3D, comparable to how glioblastoma grows in the brain. We contend that this represents a step forward compared to conventional 2D cultures and supports the need for models that are closer to real tumor environments [64].

However, several restrictions must be acknowledged. The attenuated response to temozolomide treatment, likely due to drug absorption by the scaffold matrix or restricted diffusion, highlights the complicated interaction between drug transport and therapeutic response in 3D culture systems. Additionally, our evaluation was limited to a single cell line (U87), and comprehensive quantification of spheroid distribution was constrained by the limitations of two-photon microscopy. The lack of molecular characterization of hypoxia, proliferation, and resistance markers represents an important gap for upcoming investigations.

Passive culture systems have their limits when it comes to keeping spheroids alive for long periods, which is why adding active perfusion could help. Our bead-based scaffold is set up to work with perfusion bioreactors, microfluidic devices, and organ-on-chip setups, making it easier to improve cell survival and drug testing. Next steps should include testing additional cancer cell lines, deriving organoids from patient biopsies, incorporating immune and stromal co-cultures, and examining molecular markers.

In conclusion, our porous bead-based PU scaffold platform establishes a firm foundation for preclinical and translational glioblastoma research. With its biomimetically relevant microenvironment that supports sustained spheroid culture while remaining compatible with advanced perfusion systems, this platform provides substantial promise to improve the translational relevance of preclinical drug screening studies and to advance our understanding of glioblastoma biology.

Abbreviations

The following abbreviations are used in this manuscript:

GBM	Glioblastoma
2D	Two-dimensional
TME	Tumor microenvironment
3D	Three-dimensional
PU	Polyurethane
MCTS	Multicellular tumor spheroid
TMZ	Temozolomide
ECM	Extracellular matrix
PDX	Patient-derived xenografts
OOC	Organ-on-chip
DIW	Deionized water
PBS	Phosphate-buffered saline
DMEM	Dulbecco's Modified Eagle Medium
G’	Shear storage modulus
G”	Shear loss modulus

Declarations

Conflicts of Interest

The authors declare no conflicts of interest.

Funding

This research was supported by New York Institute of Technology, (2026) Institutional Support of Research and Creativity Grants (ISRC) to K.A.

Author Contribution

All authors were involved in various aspects of the study design, data analysis, interpretations, reviewing and drafting the manuscript . K.L.Z. wrote the manuscript, performed biological assays, imaging, and data collection and analysis. R.H. planned and supervised biological assays, writing, reviewing and editing J.C. performed primary data analysis. M.D. performed CT data collection and analysis. S.K

performed secondary data analysis. R.G. reviewing and writing. K.A. conceptualized experiments, project supervision, guidance, writing, reviewing, and editing. All authors have read and agreed to the final version of the manuscript.

Acknowledgement

We would like to thank Lars Udo-Bellner for assistance with fluorescence and two photon microscopy training as well as the Griffin's Lab at the University of Arkansas for Medical Sciences for providing the U87 MG cell line.

Data Availability

The data presented in this statement are available on request from the corresponding authors, Karrer Alghazali.

References

1. Price, M. et al. CBTRUS Statistical Report: Primary Brain and Other Central Nervous System Tumors Diagnosed in the United States in 2018–2022. *Neuro-Oncol* **27** (Supplement_4), iv1–66. 10.1093/neuonc/noaf194 (2025).
2. Roger Stupp, W. P. et al. Radiotherapy plus Concomitant and Adjuvant Temozolomide for Glioblastoma. *N Engl. J. Med.* **352** (10), 987–996. 10.1056/NEJMoa043330 (2005).
3. Hanif, F., Muzaffar, K., Perveen, Malhi, S. M. & Simjee, S. U. Glioblastoma Multiforme: A Review of its Epidemiology and Pathogenesis through Clinical Presentation and Treatment. *Asian Pac. J. Cancer Prev.* **18** (1), 3–9. 10.22034/apjcp.2017.18.1.3 (2017).
4. Dymova, M. A., Kuligina, E. V. & Richter, V. A. Molecular Mechanisms of Drug Resistance in Glioblastoma. *Int. J. Mol. Sci.* **22** (12), 6385 (2021).
5. Pampaloni, F., Reynaud, E. G. & Stelzer, E. H. K. The third dimension bridges the gap between cell culture and live tissue. *Nat. Rev. Mol. Cell. Biol.* **8** (10), 839–845. 10.1038/nrm2236 (2007).
6. Sun, Y. et al. Dynamic Evolution of the Tumor Immune Microenvironment in Malignant Tumors and Emerging Therapeutic Paradigms. MedComm. 2025;6(12):e70496. (2020). 10.1002/mco2.70496 PubMed Central PMCID: PMC12674091.
7. Fontoura, J. C. et al. Comparison of 2D and 3D cell culture models for cell growth, gene expression and drug resistance. *Mater. Sci. Eng. C Mater. Biol. Appl.* **107**, 110264. 10.1016/j.msec.2019.110264 (2020).
8. Imamura, Y. et al. Comparison of 2D- and 3D-culture models as drug-testing platforms in breast cancer. *Oncol. Rep.* **33** (4), 1837–1843. 10.3892/or.2015.3767 (2015).

9. Zhou, Y., Yu, F., Guo, M., Tang, Y. & Xu, Q. Bridging the gap: the role of 3D cell cultures in mimicking tumor microenvironment for enhanced drug testing accuracy. *Front. Bioeng. Biotechnol.* 13–2025. 10.3389/fbioe.2025.1498141 (2025).
10. Ruiz-Garcia, H., Alvarado-Estrada, K., Schiapparelli, P., Quinones-Hinojosa, A. & Trifiletti, D. M. Engineering Three-Dimensional Tumor Models to Study Glioma Cancer Stem Cells and Tumor Microenvironment. *Front. Cell. Neurosci.* 14–2020. 10.3389/fncel.2020.558381 (2020).
11. Caliari, S. R. & Burdick, J. A. A practical guide to hydrogels for cell culture. *Nat. Methods*. **13** (5), 405–414. 10.1038/nmeth.3839 (2016).
12. Ahmad, Z. et al. Versatility of Hydrogels: From Synthetic Strategies, Classification, and Properties to Biomedical Applications. *Gels* **8** (3), 167 (2022).
13. Karakaya, M., Karataş, R. B., Ayaz, F. & Aydemir, E. Hydrogel applications in tumor microenvironment modeling. *Discov Biotechnol.* **2** (1), 21. 10.1007/s44340-025-00029-8 (2025).
14. Rape, A. D., Zibinsky, M., Murthy, N. & Kumar, S. A synthetic hydrogel for the high-throughput study of cell–ECM interactions. *Nat. Commun.* **6** (1), 8129. 10.1038/ncomms9129 (2015).
15. Tibbitt, M. W. & Anseth, K. S. Hydrogels as extracellular matrix mimics for 3D cell culture. *Biotechnol. Bioeng.* **103** (4), 655–663. 10.1002/bit.22361 (2009). PubMed Central PMCID: PMC2997742.
16. Segneanu, A. E. et al. Advancements in Hydrogels: A Comprehensive Review of Natural and Synthetic Innovations for Biomedical Applications. *Polymers* **17** (15), 2026 (2025).
17. Didwischus, N., Guduru, A., Badylak, S. F. & Modo, M. In vitro dose-dependent effects of matrix metalloproteinases on ECM hydrogel biodegradation. *Acta Biomater.* **174**, 104–115. 10.1016/j.actbio.2023.12 (2024). .003 PubMed Central PMCID: PMC10775082.
18. Pinto, B., Henriques, A. C., Silva, P. M. A. & Bousbaa, H. Three-Dimensional Spheroids as In Vitro Preclinical Models for Cancer Research. *Pharmaceutics* **12** (12), 1186 (2020).
19. Ryu, N. E., Lee, S. H. & Park, H. Spheroid Culture System Methods and Applications for Mesenchymal Stem Cells. *Cells* **8** (12), 1620 (2019).
20. Mitrakas, A. G. et al. Applications and Advances of Multicellular Tumor Spheroids: Challenges in Their Development and Analysis. *Int. J. Mol. Sci.* **24** (8), 6949 (2023).
21. Ahmad Zawawi, S. S., Salleh, E. A. & Musa, M. Spheroids and organoids derived from colorectal cancer as tools for in vitro drug screening. *Explor. Target. Antitumor Ther.* **5** (2), 409–431. 10.37349/etat.2024.00226 (2024). PubMed Central PMCID: PMC11090692.
22. Das, M. et al. Abstract 2104: 3D spheroid: A rapid drug screening model for epigenetic clinical targets against heterogenic cancer stem cells. *Cancer Res.* **81** (13_Supplement), 2104–2104. 10.1158/1538-7445.Am2021-2104 (2021).
23. Habra, K., Pearson, J. R. D. & McArdle, S. E. B. Robust formation of optimal single spheroids towards cost-effective in vitro three-dimensional tumor models. *FEBS Open. Bio*. **13** (7), 1266–1277. 10.1002/2211-5463 (2023). 13614 PubMed Central PMCID: PMC10315810.

24. Bach, C. et al. Rapid and reproducible generation of glioblastoma spheroids for high-throughput drug screening. *Front. Bioeng. Biotechnol.* 12–2024. 10.3389/fbioe.2024.1471012 (2024).
25. Tidwell, T. R., Røsland, G. V., Tronstad, K. J., Søreide, K. & Hagland, H. R. Metabolic flux analysis of 3D spheroids reveals significant differences in glucose metabolism from matched 2D cultures of colorectal cancer and pancreatic ductal adenocarcinoma cell lines. *Cancer Metab.* **10** (1), 9. 10.1186/s40170-022- (2022). 00285-w PubMed Central PMCID: PMC9109327.
26. Fang, Z., Li, P., Du, F., Shang, L. & Li, L. The role of organoids in cancer research. *Exp. Hematol. Oncol.* **12** (1), 69. 10.1186/s40164-023-00433- (2023). y PubMed Central PMCID: PMC10401879.
27. Marshall, L. J., Triunfol, M. & Seidle, T. Patient-Derived Xenograft vs. Organoids: A Preliminary Analysis of Cancer Research Output, Funding and Human Health Impact in 2014–2019. *Animals* **10** (10), 1923 (2020).
28. Jacob, F. et al. A Patient-Derived Glioblastoma Organoid Model and Biobank Recapitulates Inter- and Intra-tumoral Heterogeneity. *Cell* **180** (1), 188–204e22. 10.1016/j.cell.2019 (2020). 11.036 PubMed Central PMCID: PMC7556703.
29. Gao, D. et al. Organoid Cultures Derived from Patients with Advanced Prostate Cancer. *Cell* **159** (1), 176–187. 10.1016/j.cell.2014.08.016 (2014).
30. Fumagalli, A. et al. Genetic dissection of colorectal cancer progression by orthotopic transplantation of engineered cancer organoids. *Proc. Natl. Acad. Sci.* **114** (12), E2357–E2364. 10.1073/pnas.1701219114 (2017).
31. Sachs, N. et al. A Living Biobank of Breast Cancer Organoids Captures Disease Heterogeneity. *Cell* **172** (1–2), 373–386e10. 10.1016/j.cell.2017.11.010 (2018).
32. Yan, H. H. N. et al. A Comprehensive Human Gastric Cancer Organoid Biobank Captures Tumor Subtype Heterogeneity and Enables Therapeutic Screening. *Cell. Stem Cell.* **23** (6), 882–897e11. 10.1016/j.stem.2018.09.016 (2018).
33. Bose, S., Clevers, H. & Shen, X. Promises and Challenges of Organoid-Guided Precision Medicine. *Med* **2** (9), 1011–1026. 10.1016/j.medj.2021.08 (2021). .005 PubMed Central PMCID: PMC8492003.
34. Lu, T., Li, Y. & Chen, T. Techniques for fabrication and construction of three-dimensional scaffolds for tissue engineering. *Int. J. Nanomed.* **8**, 337–350. 10.2147/ijn.S (2013). 38635 PubMed Central PMCID: PMC3551462.
35. Vesvoranan, O., Anup, A. & Hixon, K. R. Current Concepts and Methods in Tissue Interface Scaffold Fabrication. *Biomimetics* **7** (4), 151 (2022).
36. Rijal, G. & Li, W. A versatile 3D tissue matrix scaffold system for tumor modeling and drug screening. *Sci. Adv.* **3** (9), e1700764. 10.1126/sciadv.1700764 (2017).
37. Sriramakrishnan, J., Kedar Ganla, R., Natarajan, K. & Selvaraj, S. A synergistic review of bioreactor technologies and their integration in 3D bioprinting. *Cogent Eng.* **12** (1), 2570724. 10.1080/23311916.2025.2570724 (2025).
38. Appel, A. A., Anastasio, M. A., Larson, J. C. & Brey, E. M. Imaging challenges in biomaterials and tissue engineering. *Biomaterials* **34** (28), 6615–6630. 10.1016/j.biomaterials.2013.05.033 (2013).

PubMed Central PMCID: PMC3799904.

39. Regmi, S., Poudel, C., Adhikari, R. & Luo, K. Q. Applications of Microfluidics and Organ-on-a-Chip in Cancer Research. *Biosens. Basel*. **12** (7). 10.3390/bios12070459 (2022). PubMed Central PMCID: PMC9313151.
40. Rogal, J., Schlünder, K. & Loskill, P. Developer's Guide to an Organ-on-Chip Model. *ACS Biomater. Sci. Eng.* **8** (11), 4643–4647. 10.1021/acsbiomaterials.1c01536 (2022).
41. Kantawala, B. et al. Revolutionizing neurotherapeutics: blood-brain barrier-on-a-chip technologies for precise drug delivery. *Ann. Med. Surg. Lond.* **86** (5), 2794–2804. 10.1097/ms9 (2024). 0000000000001887 PubMed Central PMCID: PMC11060226.
42. Li, Q., Tong, Z. & Mao, H. Microfluidic Based Organ-on-Chips and Biomedical Application. *Biosens. Basel*. **13** (4). 10.3390/bios13040436 (2023). PubMed Central PMCID: PMC10136226.
43. Sontheimer-Phelps, A., Hassell, B. A. & Ingber, D. E. Modelling cancer in microfluidic human organs-on-chips. *Nat. Rev. Cancer*. **19** (2), 65–81. 10.1038/s41568-018-0104-6 (2019).
44. Bhat, S. M. et al. 3D tumor angiogenesis models: recent advances and challenges. *J. Cancer Res. Clin. Oncol.* **147** (12), 3477–3494. 10.1007/s00432-021-03814-0 (2021).
45. Pape, J., Emberton, M. & Cheema, U. 3D Cancer Models: The Need for a Complex Stroma, Compartmentalization and Stiffness. *Front. Bioeng. Biotechnol.* 9–2021. 10.3389/fbioe.2021.660502 (2021).
46. Cordeiro, S. et al. Breaking the mold: 3D cell cultures reshaping the future of cancer research. *Front. Cell. Dev. Biol.* 12–2024. 10.3389/fcell.2024.1507388 (2024).
47. Procès, A., Luciano, M., Kalukula, Y., Ris, L. & Gabriele, S. Multiscale Mechanobiology in Brain Physiology and Diseases. *Front. Cell. Dev. Biol.* 10–2022. 10.3389/fcell.2022.823857 (2022).
48. Alves, S. R., Calori, I. R., Bi, H. & Tedesco, A. C. Characterization of glioblastoma spheroid models for drug screening and phototherapy assays. *OpenNano* **9**, 100116. https://doi.org/10.1016/j.onano.2022.100116 (2023).
49. Browning, A. P. et al. Quantitative analysis of tumour spheroid structure. *Elife* **10** 10.7554/ (2021). eLife.73020 PubMed Central PMCID: PMC8741212.
50. Grimes, D. R. & Currell, F. J. Oxygen diffusion in ellipsoidal tumour spheroids. *J. R Soc. Interface*. **15** (145). 10.1098/rsif.2018.0256 (2018).
51. Bruns, J., Egan, T., Mercier, P. & Zustiak, S. P. Glioblastoma spheroid growth and chemotherapeutic responses in single and dual-stiffness hydrogels. *Acta Biomater.* **163**, 400–414. 10.1016/j.actbio.2022.05.048 (2023).
52. Xia, H. et al. Temozolomide in Combination With NF-κB Inhibitor Significantly Disrupts the Glioblastoma Multiforme Spheroid Formation. *IEEE Open. J. Eng. Med. Biol.* **1**, 9–16. 10.1109/OJEMB.2019.2962801 (2020).
53. Chiariello, M., Inzalaco, G., Barone, V. & Gherardini, L. Overcoming challenges in glioblastoma treatment: targeting infiltrating cancer cells and harnessing the tumor microenvironment. *Front. Cell.*

Neurosci. 17–2023. 10.3389/fncel.2023.1327621 (2023).

54. Delattre, L. et al. The role of pore size and mechanical properties on the accumulation, retention and distribution of F98 glioblastoma cells in macroporous hydrogels. *Biomed. Mater.* **19** (4), 045041. 10.1088/1748-605X/ad581b (2024).
55. Palamà, I. E., D'Amone, S. & Cortese, B. Microenvironmental Rigidity of 3D Scaffolds and Influence on Glioblastoma Cells: A Biomaterial Design Perspective. *Front. Bioeng. Biotechnol.* **6** 10.3389/fbioe.2018.00131 (2018).
56. Wang, C., Tong, X. & Yang, F. Bioengineered 3D Brain Tumor Model To Elucidate the Effects of Matrix Stiffness on Glioblastoma Cell Behavior Using PEG-Based Hydrogels. *Mol. Pharm.* **11** (7), 2115–2125. 10.1021/mp5000828 (2014).
57. Kondapaneni, R. V. et al. Glioblastoma mechanobiology at multiple length scales. *Biomater. Adv.* **160**, 213860. 10.1016/j.bioadv.2024.213860 (2024).
58. Erkoc, P., Seker, F., Bagci-Onder, T. & Kizilel, S. Gelatin Methacryloyl Hydrogels in the Absence of a Crosslinker as 3D Glioblastoma Multiforme (GBM)-Mimetic Microenvironment. *Macromol. Biosci.* **18** (3). 10.1002/mabi.201700369 (2018).
59. Mansouri, M. & Leipzig, N. D. Advances in removing mass transport limitations for more physiologically relevant in vitro 3D cell constructs. *Biophys. Rev. Melville*. **2** (2), 021305. 10.1063/5.0048837 (2021). PubMed Central PMCID: PMC10903443.
60. Schmid, J. et al. A Perfusion Bioreactor System for Cell Seeding and Oxygen-Controlled Cultivation of Three-Dimensional Cell Cultures. *Tissue Eng. Part. C Methods*. **24** (10), 585–595. 10.1089/ten (2018). .TEC.2018.0204 PubMed Central PMCID: PMC6208160.
61. Gaebler, D., Hachey, S. J. & Hughes, C. C. W. Improving tumor microenvironment assessment in chip systems through next-generation technology integration. *Front. Bioeng. Biotechnol.* 12–2024. 10.3389/fbioe.2024.1462293 (2024).
62. Roy, S. M. et al. Kinetics of Nanomedicine in Tumor Spheroid as an In Vitro Model System for Efficient Tumor-Targeted Drug Delivery With Insights From Mathematical Models. *Front. Bioeng. Biotechnol.* 9–2021. 10.3389/fbioe.2021.785937 (2021).
63. Erickson, A. E., Lan Levengood, S. K., Sun, J., Chang, F. C. & Zhang, M. Fabrication and Characterization of Chitosan–Hyaluronic Acid Scaffolds with Varying Stiffness for Glioblastoma Cell Culture. *Adv. Healthc. Mater.* **7** (15), 1800295. 10.1002/adhm.201800295 (2018).
64. Manikandan, C. & Jaiswal, A. K. Scaffold-based spheroid models of glioblastoma multiforme and its use in drug screening. *Biotechnol. Bioeng.* **120** (8), 2117–2132. 10.1002/bit.28481 (2023).

Figures

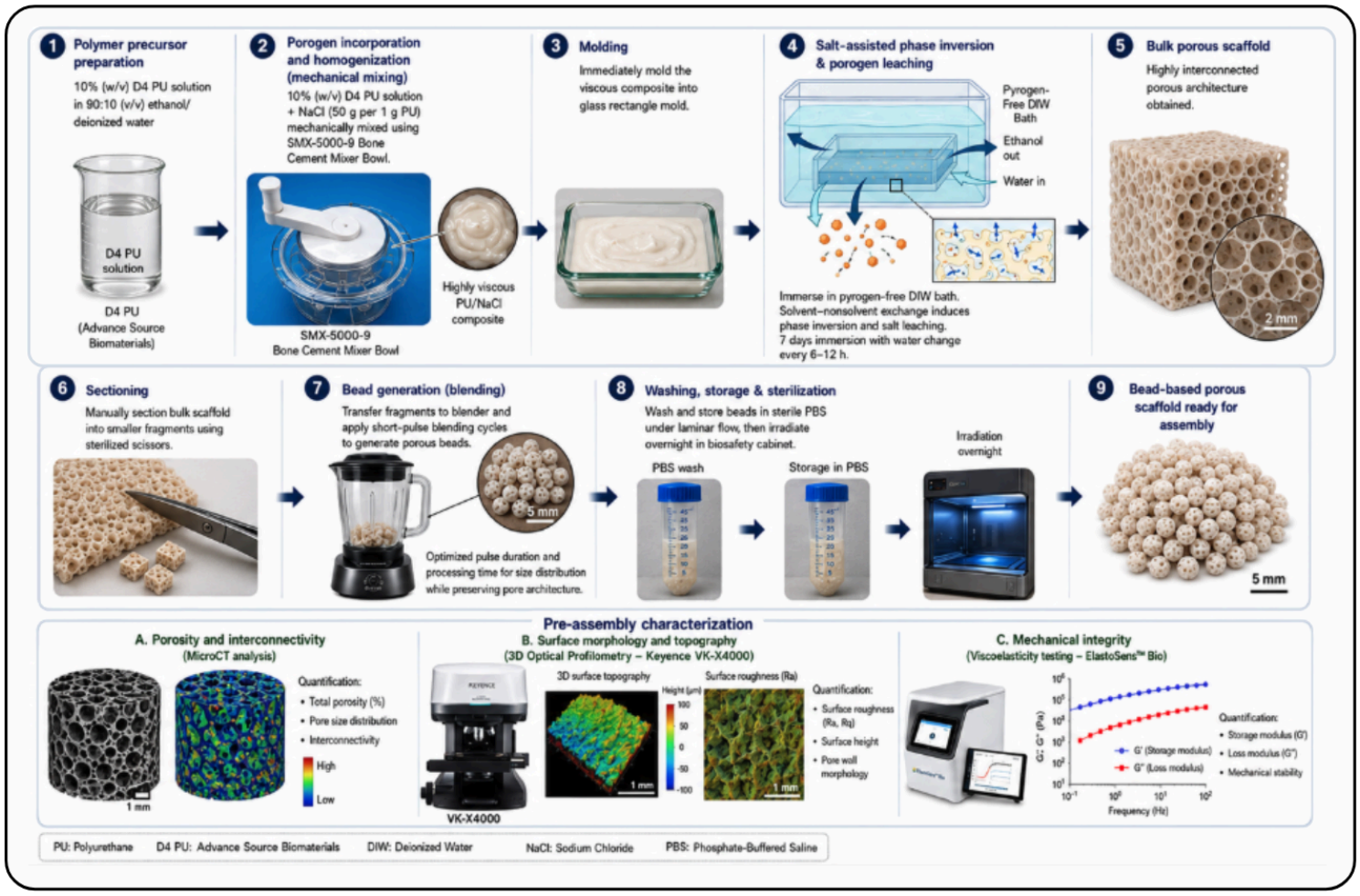


Figure 1

Fabrication workflow and pre-assembly characterization of porous polyurethane (PU) beads. A 10% (W/V) D4 PU solution was mechanically integrated with NaCl (50g/1g PU) using a SMX-5000-9 Bone Cement Mixer Bowel and packed into glass molds. Porous scaffolds were generated through salt-assisted phase inversion and porogen leaching in pyrogen-free DIW, followed by sectioning and blending to produce porous beads. Prior to assembly, beads were washed, sterilized, and stored in PBS. Pre-assembly characterization included A) Analysis with MicroCT for porosity and interconnectivity, B) Assessment with 3D Optical Profilometry for surface morphology and topography, and C) Analysis with ElastoSens^{TM} Bio for viscoelasticity.

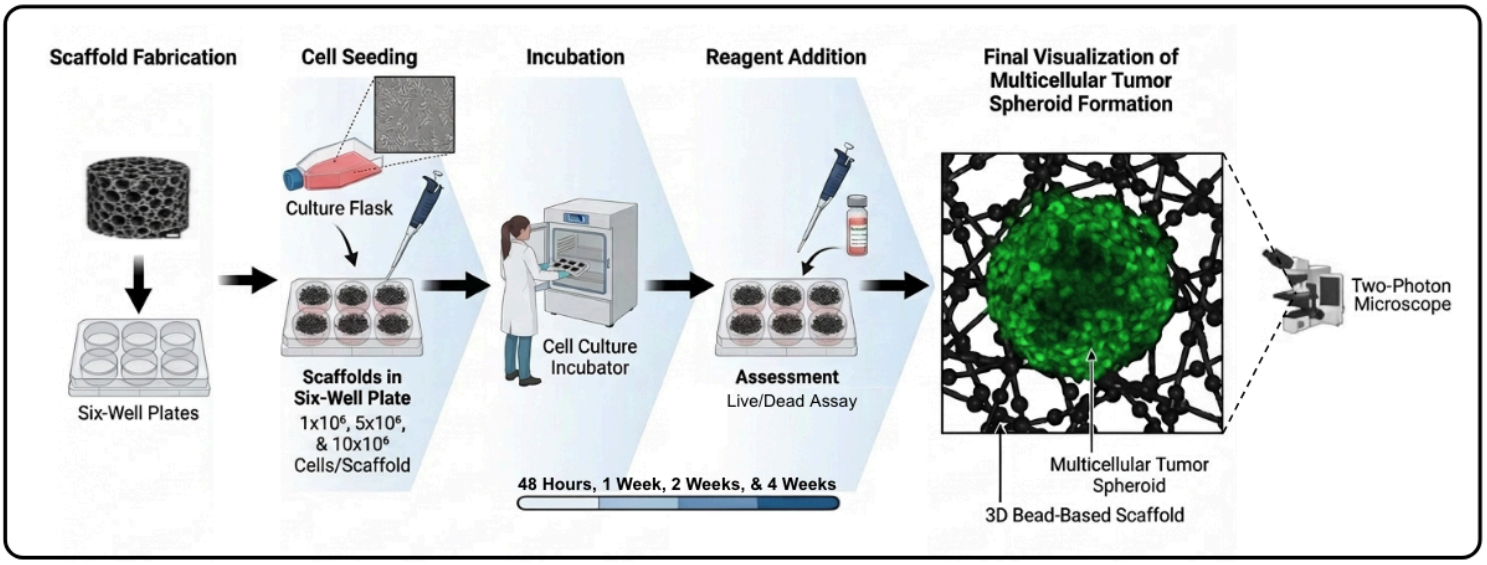


Figure 2

Experimental workflow for multicellular tumor spheroid generation

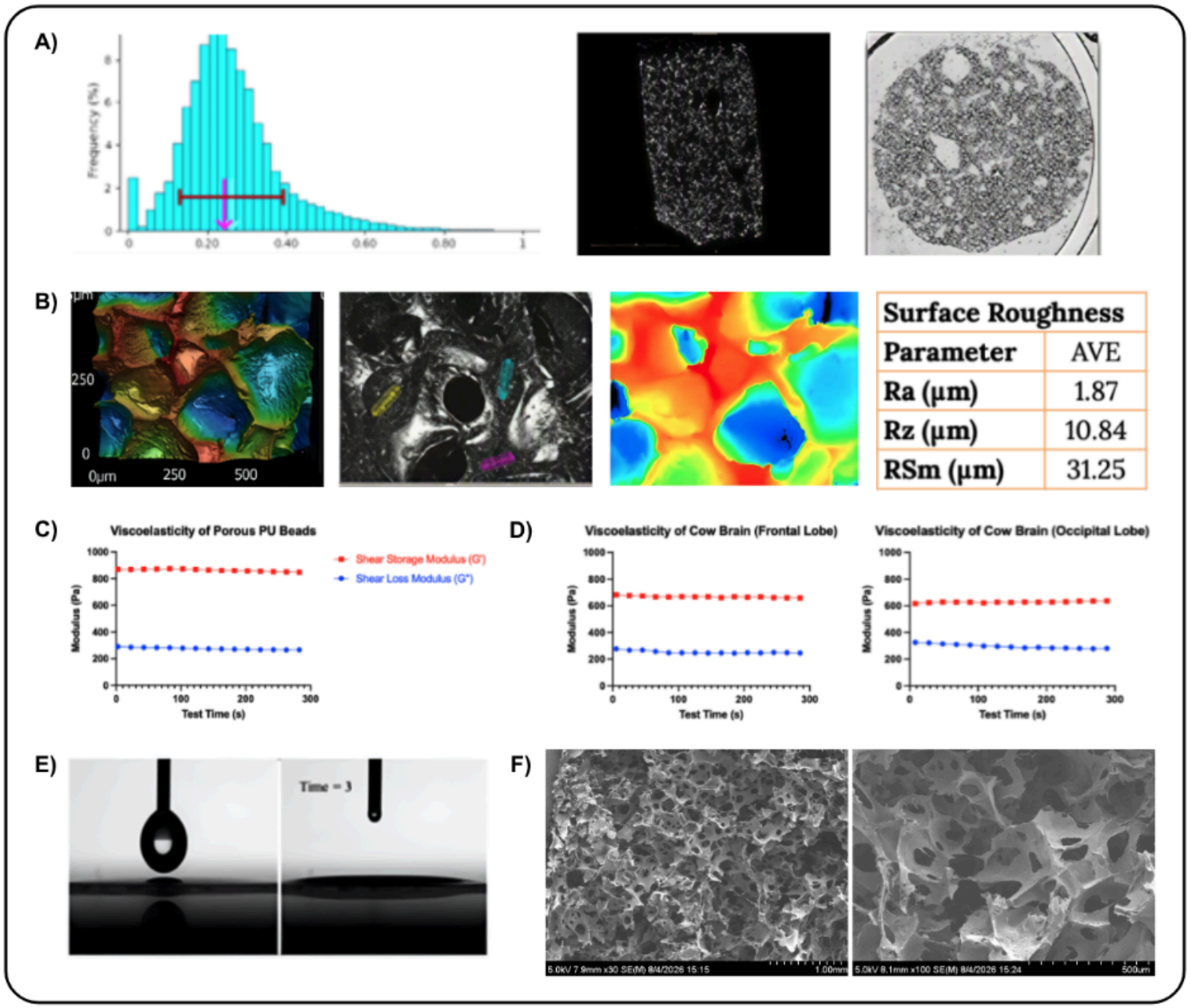


Figure 3

Comprehensive characterization of polyurethane (PU) beads. A) Internal pore architecture, porosity, and interconnectivity were analyzed using Micro-Computed Tomography (Bruker SkyScan 1173). B) Surface morphology and roughness were evaluated using 3D Optical Profilometry (Keyence VK-X4000), providing quantitative measurements of Ra, Rz, and RSm. C) Mechanical stiffness and shear storage modulus (G') were analyzed using Viscoelasticity Testing (ElastoSens Bio). D) Viscoelasticity Testing (Elastosens Bio) was performed on sheep brain tissue for comparison with the beads. E) Surface wettability was assessed through static water contact angle goniometry. (F) Surface topography was analyzed with scanning electron microscopy (SEM), with low-magnification imaging (30x) demonstrating a uniformly distributed, interconnected porous network and high-magnification imaging (100x) revealing thin polymer walls, interconnected pore windows, and a rough surface morphology.

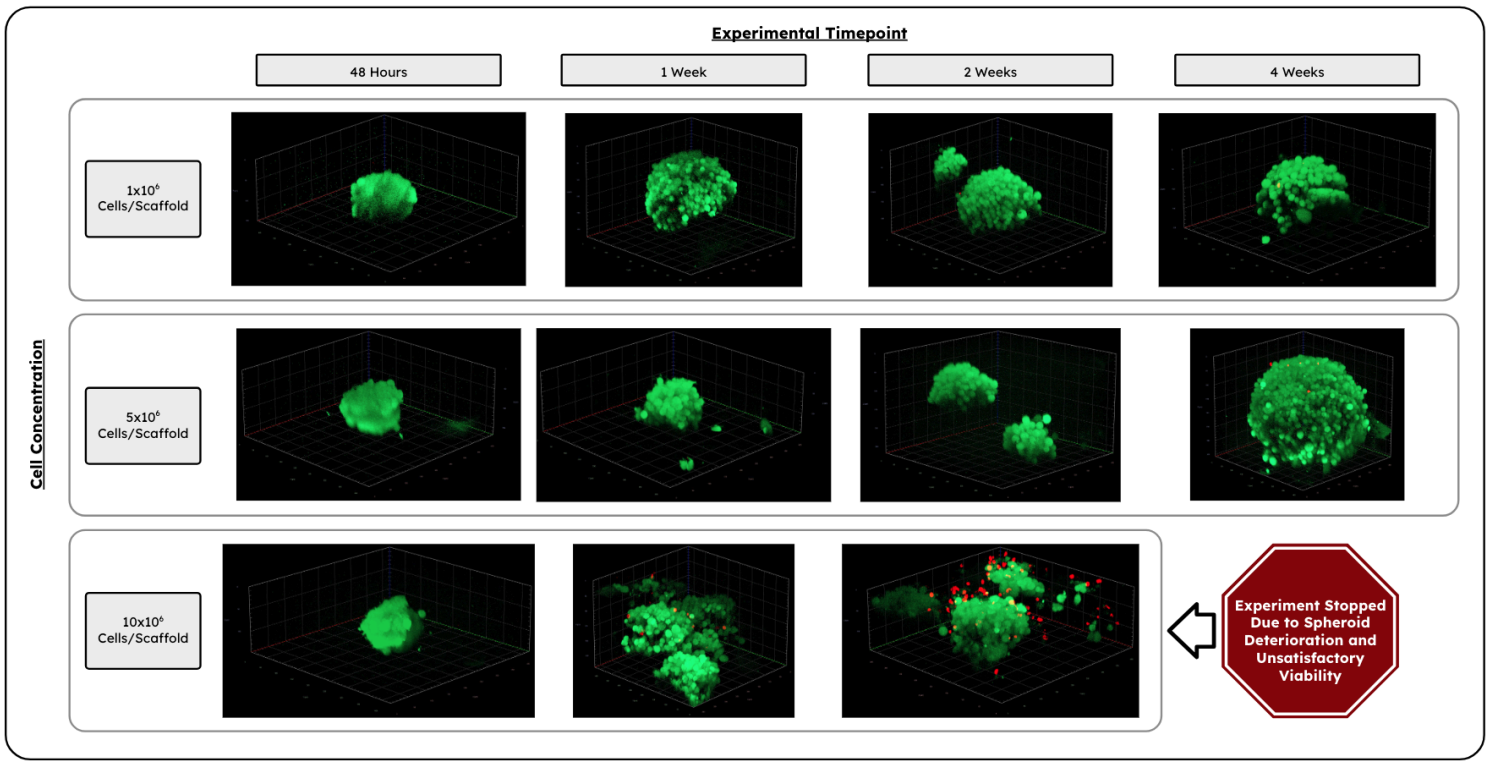


Figure 4

Representative three-dimensional (3D) reconstructions of U87 glioblastoma spheroids generated from two-photon z-stack images across experimental concentrations and timepoints. Live Cells: Calcein-AM (Green); Dead Cells: Ethidium Homodimer-1 (Red).

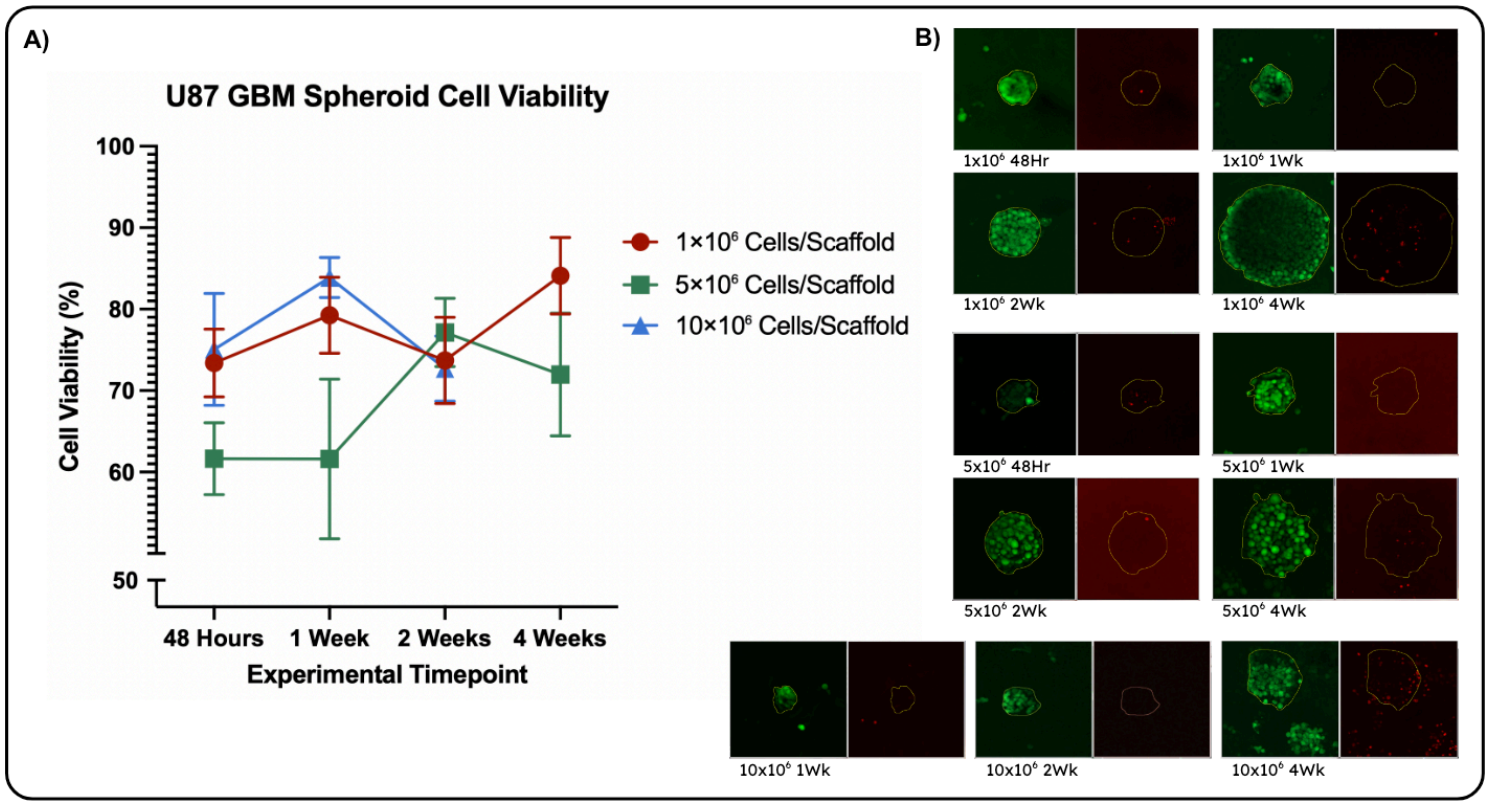


Figure 5

Cell viability of U87 GBM spheroids over experimental timepoints and across cell seeding concentrations. A) Quantification of cell viability (%) at 48Hr, 1Wk, 2Wk, and 4Wks for spheroids seeded at $1x10^6$ (Red), $5x10^6$ (Green), and $10x10^6$ (Blue) Cells per Scaffold. Data are presented as mean ± SD. B) Live/Dead fluorescence images of spheroids at each timepoint and concentration. The yellow outlines indicate manually defined spheroid boundaries utilized for calculation of cell viability values.

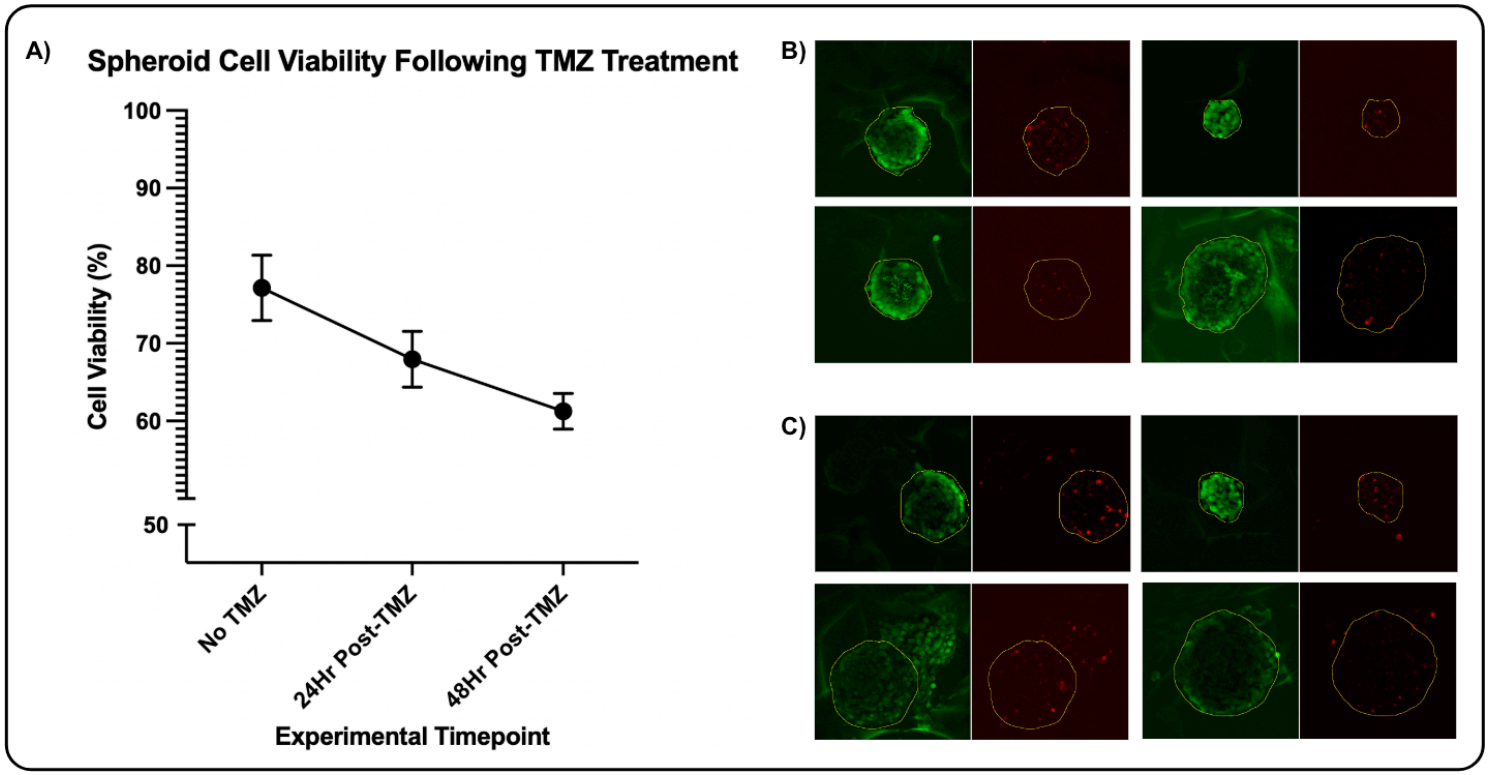


Figure 6

Administration of temozolomide (TMZ) induces moderate cytotoxicity to spheroids, with progressive effects on cell viability observed at 24Hr and 48Hr. A) Quantification of cell viability (%) at 24Hr and 48Hr following treatment of scaffolds with TMZ. B) Live/Dead fluorescence images of spheroids at 24Hr. C) Live/Dead fluorescence images of spheroids at 48Hr.